Supporting Information for:

Quantum Transport and Band Structure Evolution under High Magnetic Field in Few-layer Tellurene

Gang Qiu[1,2], Yixiu Wang[3], Yifan Nie[4], Yongping Zheng[4], Kyeongjae Cho[4], Wenzhuo Wu[2,3],

Peide D. Ye[1,2]*,

[1]School of Electrical and Computer Engineering, Purdue University, West Lafayette, Indiana 47907, USA

[2]Birck Nanotechnology Center, Purdue University, West Lafayette, Indiana 47907, USA

[3]School of Industrial Engineering, Purdue University, West Lafayette, Indiana 47907, USA

[4]Department of Materials Science and Engineering, the University of Texas at Dallas, Richardson, Texas 75080, United States

*e-mail: Correspondence and requests for materials should be addressed to P. D. Y. (email: yep@purdue.edu Phone: (765)-494-7611)

Supporting Note 1: Density functional theory (DFT) calculations

The density functional theory (DFT) calculations are performed in two parts. The structural optimization of the crystal structure is performed with the Vienna ab-initio Simulation Packages (VASP)[1], with the projector-augmented wave (PAW) method[2]. The wave functions are expanded into plane waves with an energy cut-off of 400 eV. Exchange-correlation interactions are described by the generalized gradient approximation (GGA) using the Perdew-Burke-Ernzerhof (PBE) functional[3]. A Γ-centered 8x8x8 k-point sampling mesh is adopted in the integration in the first Brillouin zone. The convergence criteria for electron and ionic minimization are 10^{-4} eV and 10^{-2} eV/Å, respectively. For a better description of the electronic structures, the band structure calculation is performed with WIEN2K[4], using the modified Becke-Johnson local-density approximation (MBJLDA) exchange functionals[5]. Spin-orbit coupling is implemented in the calculation, with a Γ-centered 12x12x12 k-point mesh. To calculate the electronic band structure change under external magnetic field, the spin up and spin down exchange correlation potentials are shifted by $\pm \mu_B B_{ext}$, respectively[6]. The external magnetic field is normal to the helix axis.

Supporting Note 2: Te band structure from DFT calculations
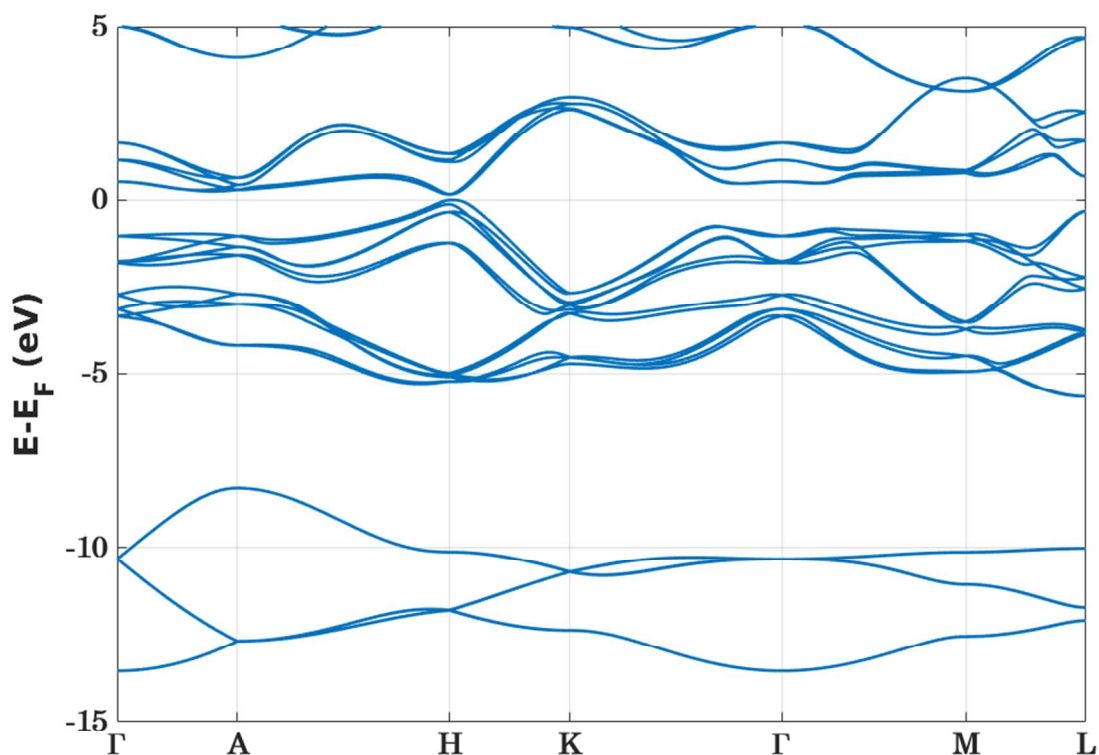
Figure S1. Full electronic structure of bulk Te calculated from DFT methods as discussed in Note 3.

Supporting Note 3: Synthesis Method of Large-area Tellurene Nano-films

The synthesis of tellurene nano-films follows the procedure described in the previous literature[7]. 0.09 g of Na_2TeO_3 and 0.50 g of poly (vinyl pyrrolidone) (PVP, M.W.= 58000) were put into a 50 mL Teflon-lined stainless steel autoclave. Subsequently aqueous ammonia solution (25–28%, w/w%) and hydrazine hydrate (80%, w/w%) with the volume ratio of 2:1 were added into the mixed solution under vigorous magnetic stirring. Double-distilled water was added to 80% of the container volume. The container was then sealed and heated at 180 ^{o}C for 20 hours before cooling down to room temperature.

The freshly prepared solution with 2D Te suspension was centrifuged. After removing the supernate, N, N-dimethylformamide (DMF; 1 mL) and $CHCl_3$ (1 mL) were added into the mixture. A 50 μL syringe

was used to disperse mixed suspension containing Te flakes onto the water drop by drop. After that, the floating 2D Te can be directly scooped on the substrate.

Supporting Note 4: Device Fabrication and Characterization

Figure S1 shows the fabrication process flow for Hall bar devices. The as-grown tellurene flakes are usually in rectangular or trapezoidal shapes, with one-dimensional atomic chains ([0001] crystal orientation) aligned with the long edge of the flakes, which was studied thoroughly in previous Raman experiments[8]. After being dispersed onto 300 nm SiO_2/p++ Si substrates, the samples were cleaned by standard solvent cleaning procedure and patterned with electron beam lithography into two rectangles with identical geometry but along different primary crystal axes. The flake is then trimmed with 30 seconds of BCl_3/Ar plasma dry etching process. The purpose of this step is to eliminate the geometric non-ideality in measuring the transport anisotropy. Six-terminal Hall-bar structure was subsequently patterned by electron beam lithography again and metal contacts of 50/100 nm Pd/Au were formed by electron beam evaporator. We denote the bottom flake in Figure S2(c) as along 1D direction since the drain current flows along 1D atom chains and the top flake as vdW direction since the drain current flows along van der Waals bonds.
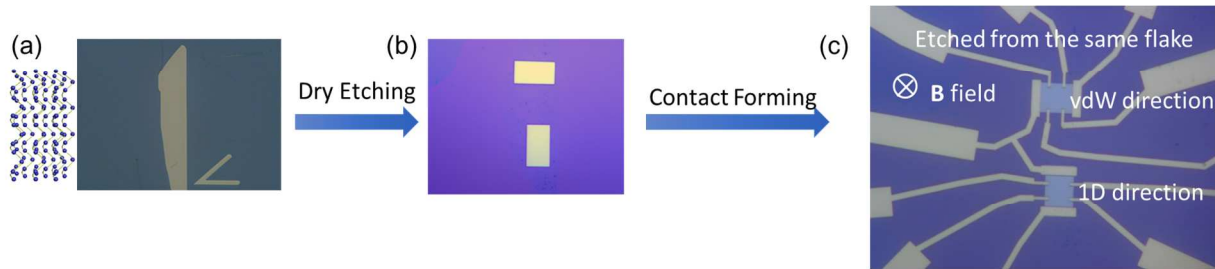

Figure S2. Process flow of fabricating Hall bar devices along different directions. The optical image of **(a)** as-grown tellurene flakes dispersed on the substrates. The 1D atomic chains are aligned with the long edge of the flake; **(b)** the flakes were trimmed into to perpendicular rectangles with BCl_3/Ar dry etching method; **(C)** Pd/Au contacts were patterned and metallized to form two Hall-bar devices.

The magneto transport measurement was carried out in a He[3] cryostat with a superconducting magnet at National High Magnetic Field Lab in Tallahassee, FL. The data was acquired from Stanford Research Instruments SR830 lock-in amplifier with standard lock-in measurement techniques, with 100 nA or 1μA injected AC current.

Supporting Note 5: Pd-Te Contact Resistance at Low Temperature

The high quality of metal-to-semiconductor contacts is essential for the soundness and reproducibility of the experiment data. Luckily for Te, the Fermi level is aligned near the edge of valence band and p-type Ohmic can be achieved by introducing high work function metal such as Pd (~5.2 eV) or Ni (~5.1 eV). Our previous results[7] showed that at room temperature the on-state Pd-Te contact resistance can be as low as 0.5 kΩ·μm (extracted from transmission line method). Furthermore, here we measured the four-terminal and two-terminal resistance of a Hall bar device with Pd contacts during the cooling down process (see Figure S3(a) below). With a homogeneous channel, the contact resistance can be roughly estimated from: $2R_c = R_{2T} - R_{4T}\frac{L}{l}$, here L is the total device length, l is the distance between two side terminals in Hall bar structure, and R_{4T}, R_{2T} are four-terminal and two-terminal resistance respectively. We found that the Pd-Te contact resistance is still moderate at low temperatures, instead of increasing exponentially as typical Schottky contacts.
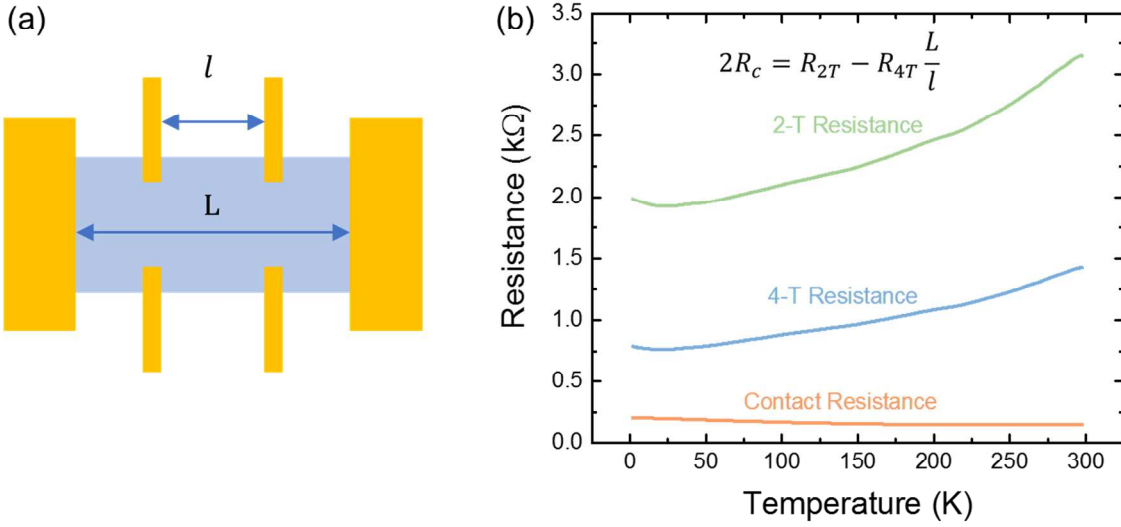
Figure S3 (a) Hall bar device structure. (b) Temperature dependence of two-terminal, four-terminal and contact resistance of a Hall bar device with Pd contacts. Contact resistance R_c is extracted from the equation $2R_c = R_{2T} - R_{4T}\frac{L}{l}$.

Supporting Note 6: Hall Measurement along 1D Direction and van der Waals Direction

The conductance ($1/R_{xx}$) along 1D direction and vdW direction was first measured under different gate bias under low temperature. The 1D direction shows about 1.3 times higher conductivity than vdW direction. Since the conductance can be expressed as $\sigma = \frac{1}{\rho_{xx}} = qn\mu$, which is proportional to the carrier density and mobility, one may intuitively reckon that the carrier density should be the same along two directions whereas the conductance discrepancy should arise from the mobility difference. We attempted to verify this presumption by conducting Hall measurement on both devices and calculate 2D carrier density n_{2D} and Hall mobility μ_{Hall} from the equations: $n_{2D} = \frac{B}{eR_{xy}}$ and $\mu_{Hall} = \frac{L}{W}\frac{1}{R_{xx}n_{2D}e}$ respectively. However, the calculated Hall mobility is similar in both devices yet the 2D carrier density varies with a ratio similar to the conductance anisotropic ratio, as shown in Figure S3(b), which conflicts with our

anticipation. In order to correctly evaluate the results from the Hall measurement, we have to retrospect the derivation of above equations in calculating 2D sheet density and Hall mobility. The root of Hall effect is the balance between Lorentz force and Coulomb force: $q\boldsymbol{v} \times \boldsymbol{B} = q\boldsymbol{E}$, where the carrier velocity is generalized with the average velocity. However, in real scenarios the distribution of velocity of electrons should follow Boltzmann distribution. For those electrons travelling faster than average velocity, the Lorentz force will be larger than Coulomb force and the trajectory of the particle will be deviated in one direction, and likewise the electrons with smaller velocity will be deviated into the other direction, as depicted in Figure S4. In other words, the Hall mobility measures average in-plane motion, so it is reasonable for both devices to have similar Hall mobility. For 2D carrier densities, if we follow the classical Boltzmann distribution and take all electrons with different velocity into account by integrating by velocity, than we shall alter the widely used formula $n_{2D} = \dfrac{B}{eR_{xy}}$ into a slight different form $n_{2D} = r_H \dfrac{B}{eR_{xy}}$, here r_H is the Hall factor which is defined as: $r_H = \dfrac{\langle \tau_m^2 \rangle}{\langle \tau_m \rangle^2}$. Since the relaxation time τ_m is a tensor, r_H contains the information of anisotropic transport. Hence, it is questionable to use Hall measurement to calibrate anisotropic transport and alternative approaches should be adopted as we will discuss in the next session.
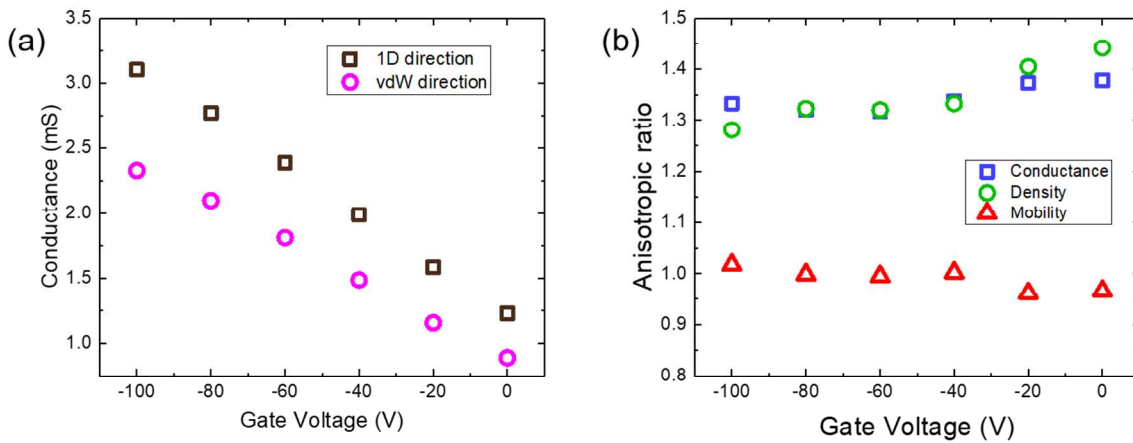
Figure S4. (a) Conductance measured under different gate bias. (b) Anisotropic ratio of conductance, 2D carrier density and Hall mobility. The 2D carrier density n_{2D} and Hall mobility μ_{Hall} from the equation:

$n_{2D} = \frac{B}{eR_{xy}}$ and $\mu_{Hall} = \frac{L}{W}\frac{1}{R_{xx}n_{2D}e}$ respectively.
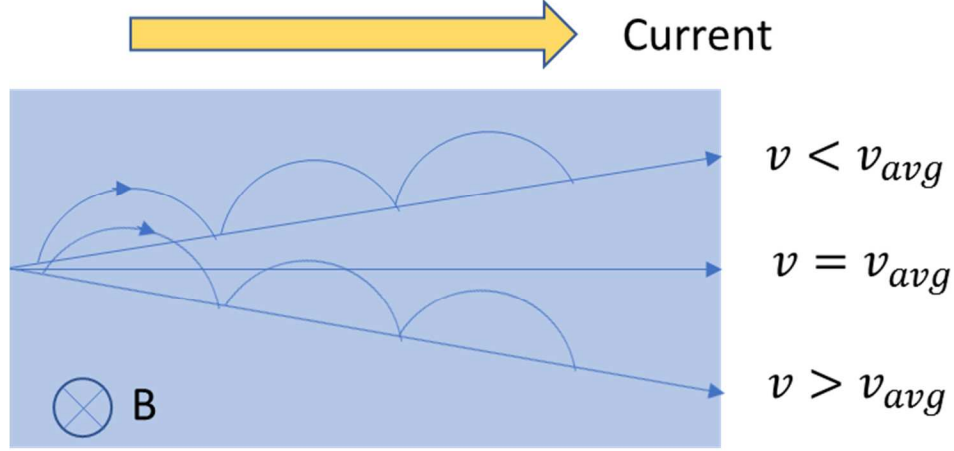

Figure S5. Schematic demonstration of velocity distribution in Hall measurement.

Supporting Note 7: Determination of Mobility Anisotropic Ratio from Magneto-Resistance

Another common practice of determining mobility is to use magneto-resistance measurement. In small magnetic field regime, the magneto-resistance (defined as $\Delta MR = \frac{\rho_B - \rho_0}{\rho_0}$) should follow a parabolic relationship with the external magnetic field: $\Delta MR = \alpha\mu^2 B^2$, where α is the magneto resistance coefficient that is only related with geometric factor. Hence for two identical devices, we can assume the coefficient α to be the same and hence by fitting the magneto resistance in B<5T regime, we can derive the mobility ratio to be $\mu_{1D}/\mu_{vdW} = 1.32$. This value is close to room temperature field-effect mobility ratio and was explained by DFT calculations.
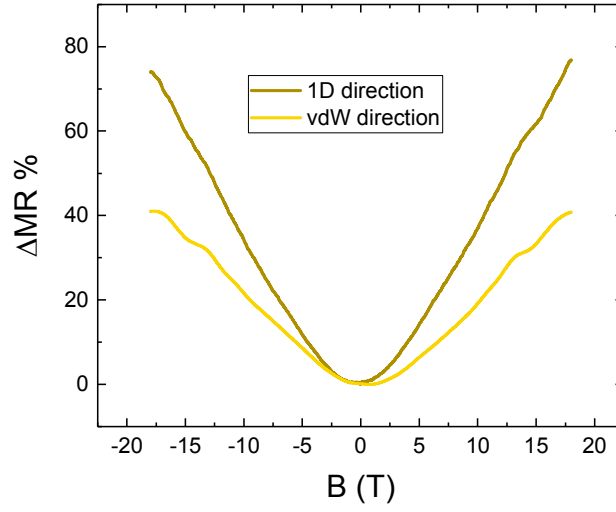
Figure S6. Magneto resistance along 1D direction and vdW direction. At small magnetic field regime (B < 5 T), the magneto resistance follows parabolic relationship with B field, from which we can extract the mobility.

Supporting Note 8: SdH Oscillations in thicker samples

We found that in another thicker sample (18 nm), the amplitude of oscillations are much weaker and only two periods can be observed. And no plateau is formed in transverse resistance, indicating much weaker quantum confinement in thicker tellurene films.
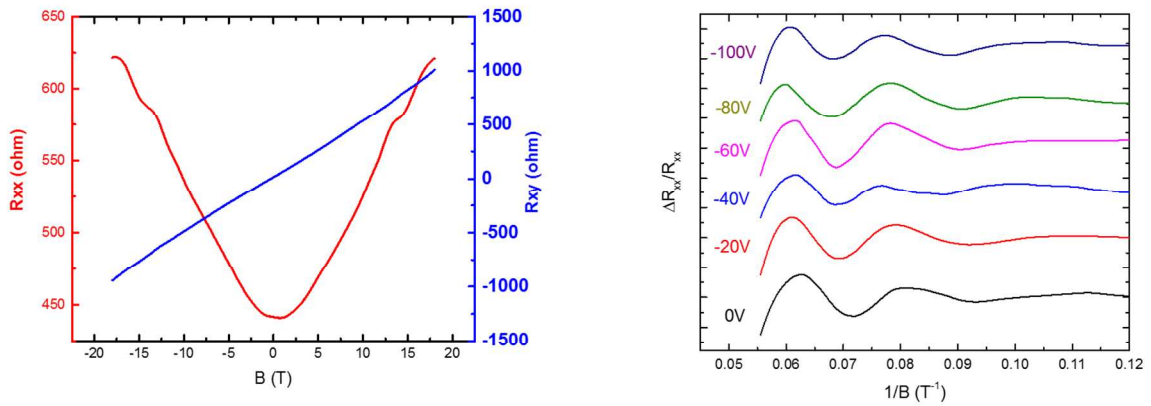
Figure S7. Shubnikov-de-Haas oscillations in an 18-nm-thick sample. The normalized oscillation features are less predominant compared to the 10-nm-thick sample, indicating weaker quantum confinement in thicker tellurene films.

Supporting Note 9: Extraction of Carrier lifetime

Carrier lifetime was extracted by fitting the oscillation amplitudes with thermal factor and Dingle factor:

$$\Delta R_{xx} \propto R_T R_D = \frac{\lambda(T)}{\sinh \lambda(T)} \times \exp(-\frac{\pi m^*}{\tau e B})$$

Where $\lambda(T) = 2\pi^2 k_B m^* T / \hbar e B$. By reformation the above equation and take the semilog plot we shall get: $\ln(\Delta R_{xx} \cdot B \cdot \sinh \lambda(T)) = -\frac{\pi m^*}{\tau e B} + const$. Therefore by plotting $\ln(\Delta R_{xx} \cdot B \cdot \sinh \lambda(T))$ against $1/B$ (Figure R4), we observe a linear trend whose slope gives us the carrier lifetime of 0.10 ps.
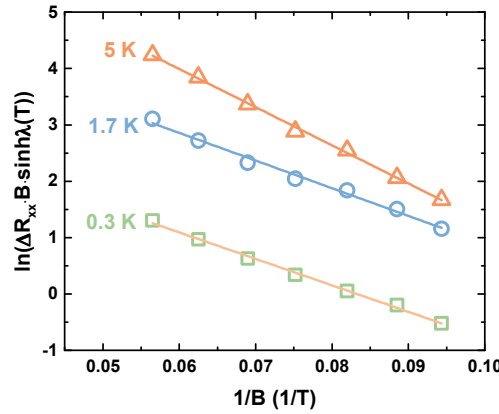

Figure S8 Dingle plots of $\ln(\Delta R_{xx} \cdot B \cdot \sinh \lambda(T))$ versus $1/B$ at different temperatures. The carrier lifetime of 0.1 ps is extracted from the slope of the plot.

1.   Kresse, G.; Furthmüller, J. Efficient iterative schemes for ab initio total-energy calculations using a plane-wave basis set. *Phys. Rev. B - Condens. Matter Mater. Phys.* **1996**, *54*, 11169–11186.

2.   Kresse, G.; Joubert., D. From ultrasoft pseudopotentials to the projector augmented-wave method. *Phys. Rev. B - Condens. Matter Mater. Phys.* **1999**, *59,* 1758–177.

3.   Perdew, J. P., Burke, K.; Ernzerhof, M. Generalized gradient approximation made simple. *Phys. Rev. Lett.* **1996**, *77,* 3865–3868.

4.   Sarkar, D., Xie, X., Liu, W., Cao, W., Kang, J., Gong, Y., Kraemer, S., Ajayan, P.M.; Banerjee, K. A subthermionic tunnel field-effect transistor with an atomically thin channel. *Nature* **526,** 91–95 (2015).

5.   Tran, F.;Blaha, P. Accurate band gaps of semiconductors and insulators with a semilocal exchange-correlation potential. *Phys. Rev. Lett.* **2009,** *102,* 5–8.

6.   Hirst, L. L. The microscopic magnetization: concept andapplication. *Rev. Mod. Phys.* **1997**, *69,* 607–628.

7.   Wang, Y., Qiu, G., Wang, R., Huang, S., Wang, Q., Liu, Y., Du, Y., Goddard, W.A., Kim, M.J., Xu, X. and Peide, D.Y. Field-effect transistors made from solution-grown two-dimensional tellurene. *Nat. Electron.* **2018**, 1, 228–236.

8.   Du, Y., Qiu, G., Wang, Y., Si, M., Xu, X., Wu, W. and Ye, P.D. One-Dimensional van der Waals Material Tellurium: Raman Spectroscopy under Strain and Magneto-Transport. *Nano Lett.* **2017,** *17,* 3965−3973.